



# Regulation on Annealing Multiscale Laminar Structure and Mechanical Characteristics of Plain Medium Carbon Steel by Warm Pre-deformation Extent

GUOLONG LIU, SHUAI LIU, DONGMEI ZHANG, YUNLI FENG,  
and FUCHENG ZHANG

A heterogeneous structure of multi-scale ferrite and granular or short rod cementite was obtained by warm-rolled pseudo-eutectoid microstructure, and the recrystallization of deformed ferrite and the dissolution and precipitation of cementite were controlled by subsequent short-time annealing treatment. The results show that the ferrite grains of annealed samples with different deformation extent distributed in the multiscale laminar structure, and the grain size trans from nanoscale to micron-scale. With the increase of deformation, the recrystallization ratio increases. The annealing sample with deformation of 84 pct obtains the optimal microstructure of multi-scale lamellar ferrite cementite that effectively improves the strain-strengthening ability, and realizes the optimal combination of strength and plasticity. The accumulation of more GNDs in a gradient distribution at the heterogeneous interface provides good strain reinforcement with the highest boundary density, which helps to provide additional strength and plasticity. The multi-stage regulation of ferrite recrystallization and cementite distribution after annealing provides good elongation to achieve a combination of HDI mechanism, fine grain strengthening, and Orowan strengthening mechanism. Various models were used to fit the true stress–true strain, and the Voce-Kocks model accurately described the stress–strain of plain medium carbon steel with a heterogeneous laminar structure.

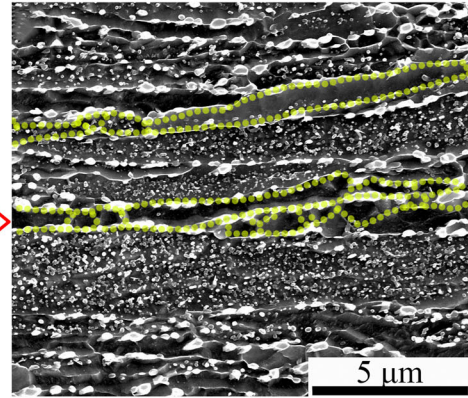
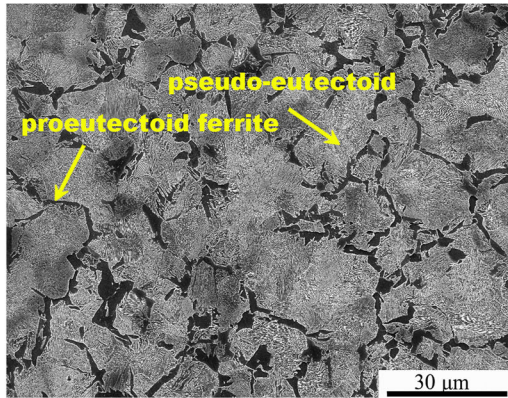
---

GUOLONG LIU, SHUAI LIU, DONGMEI ZHANG, YUNLI FENG, and FUCHENG ZHANG are with the College of Metallurgy and Energy, North China University of Science and Technology, Tangshan 063210, Hebei, P.R. China. Contact e-mail: fengyl@ncst.edu.cn

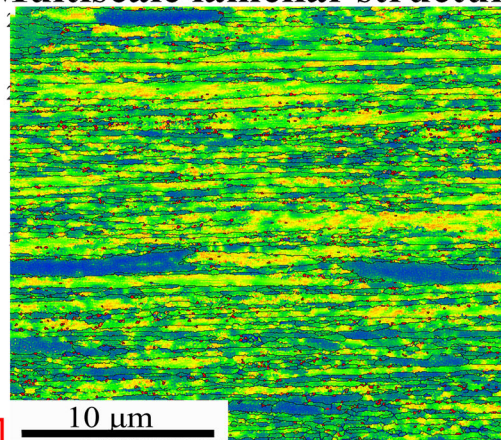
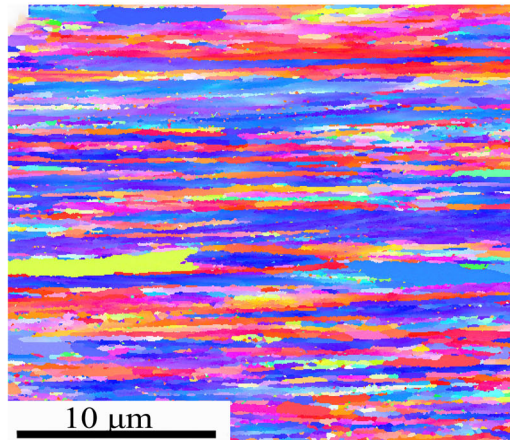
Manuscript submitted September 19, 2022; accepted January 22, 2023.

Article published online February 15, 2023

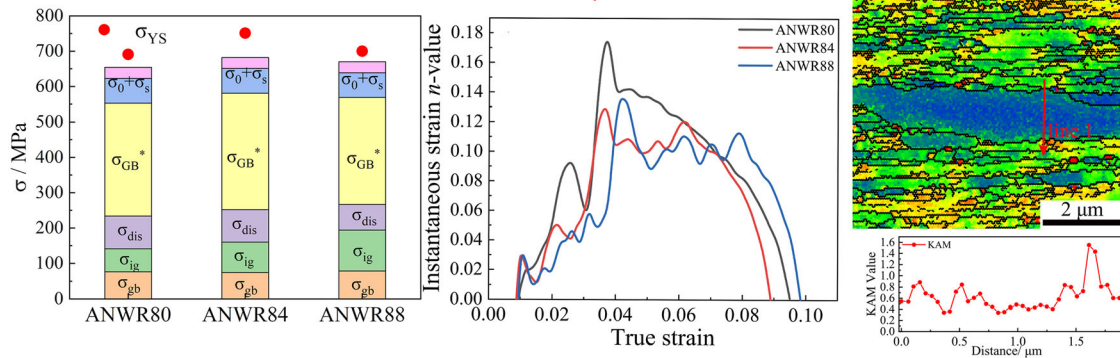
## Initial pseudoeutectoid structure



## Multiscale lamellar structure



## Additional strengthening of heterogeneous lamellar structure



<https://doi.org/10.1007/s11661-023-06992-3>

© The Minerals, Metals & Materials Society and ASM International 2023

### I. INTRODUCTION

THE iron and steel materials are the most widely used metal materials. In recent years, high strength low alloy (HSLA) steel has been widely used in industry and engineering fields due to its excellent comprehensive properties. HSLA steels are made by adding tiny

amounts of alloying elements (niobium, molybdenum, manganese, *etc.*) to plain carbon steel, combining with a heat treatment process that enhances its strength and toughness. However, the addition of alloying elements such as molybdenum and niobium not only increase the cost of the alloy, but also complicates the preparation

process and reduces the weldability of the alloy. Improving the strength of steel while reducing production costs is one of the urgent problems to be solved. The research shows that the grain refinement by large plastic deformation can greatly improve the strength of plain carbon steel, but reduce its ductility. In fact, this strength-ductility trade-off has long been a dilemmatic issue in materials science.<sup>[1]</sup> Inspiration from Luke's theory of making materials plain,<sup>[2,3]</sup> the strength and plasticity of the alloy are optimized by designing the internal microstructure of the alloy without changing the alloy composition.

The 'Making Materials Plain' method has obvious advantage over the traditional alloying optimization of metal properties. Without adding alloying elements, it not only saves the alloy cost but also is contributes to sustainable development. The construction and optimization of heterogeneous structures is an effective way to enhance the mechanical properties of materials. Thus, a variety of microstructures, such as heterogeneous lamellar structure,<sup>[4,5]</sup> gradient structure,<sup>[6]</sup> multiphase structure<sup>[7]</sup> and multimodal structure,<sup>[8]</sup> have been designed. The heterogeneous laminate structure is an optimal heterogeneous structure that allows for the best combination of strength and plasticity.<sup>[4,9-11]</sup> Wu<sup>[5]</sup> prepared pure titanium with heterogeneous lamellar structure by asynchronous rolling and annealing. The results showed that the strength and plasticity of titanium can be optimized simultaneously by adjusting the ultra-fine grain (UFG) strength and coarse grain volume ratio. Zhang *et al.*<sup>[12]</sup> achieved a complex hierarchical layer + lamella structured by stacking cold rolled IF steel plates with different grain sizes. The yield strength, tensile strength, and extensional ductility of IF steel were greatly improved, mainly due to the effect of homogeneous interface and grain distribution caused by mechanical incompatibility between the layer interface and the micro-scale sheet. The addition of lamellar structure to UFG duplex steels (ferritic/martensitic) leads to improved work-hardening capacity, resulting in high strength and good ductility.<sup>[13,14]</sup>

Accordingly, the present researches are mainly concentrated on alloy steels,<sup>[15-18]</sup> and there are no articles giving a comprehensive understanding of the annealing behavior and heterogeneous lamellar structure of plain medium carbon steel. Therefore, in the present study a plain medium carbon steel was prepared and fabricated by warm rolling and annealing treatment to obtain heterogeneous lamellar structure. The annealing behavior and tensile properties of warm rolled samples with different deformation were studied by electron back scatter diffraction (EBSD), transmission electron microscopy (TEM) and room temperature tensile test. The hardening behavior of heterogeneous lamellar structure after annealing was discussed. In addition, according to the size and distribution of cementite, the coefficient related to grain boundary cementite is proposed to correct the grain size, which confirms the existence of an additional strengthening mechanism. The function model of true stress and true strain of

heterogeneous lamellar structure of plain medium carbon steel is fitted.

## II. EXPERIMENTAL MATERIALS AND METHODS

The plain medium carbon steel bar was selected, and the chemical composition was 0.46 pct C, 0.60 pct Mn, 0.28 pct Si, 0.019 pct S, 0.02 pct P (wt pct). A number of rectangular samples with sizes of 12 mm × 12 mm × 100 mm, 15 mm × 15 mm × 100 mm and 20 mm × 20 mm × 100 mm were cut by wire cutter for subsequent heat treatment and warm rolling. The sample was heated to 870 °C in the furnace and kept for 45 minutes to austenitized at low temperature. The samples are cooled at room temperature water-cooled to form martensite, while in air-cooled to form pearlite. The previous quenching experiments showed that when the water temperature was lower than 90 °C, the percentage of primary ferrite (island distribution) was lower, while the percentage of primary ferrite was higher when the water temperature was higher than 90 °C. Only the water temperature was 90 °C with a cooling rate of ~ 24°C/s, the primary ferrite, mainly with banded, distributed along the pearlite boundary was obtained. Such a microstructure is beneficial to obtaining a multi-scale structure after warm rolling. Thus, the sample was taken and quickly immersed in water at 90 °C for quenching to obtain a pseudo-eutectoid structure.

The pretreated sample was heated to 550 °C for 15 minutes at a heating rate of 15 °C/min, and then warm-rolled with total deformations of 80, 84 and 88 pct respectively. The final thickness of the warm rolled sample was ~ 2.4 mm. The warm rolled sample was reheated to 600 °C for 30 minutes and then cooled to room temperature. The annealed samples are defined as ANWR80, ANWR84 and ANWR88. The microstructure of the samples was characterized by the FEI Quanta-650 FEG field emission scanning electron microscope (SEM) equipped with EBSD. The samples for EBSD were electropolishing, and the polishing solution was 80% ethanol + 15 pct perchloric acid + 5 pct glycerol (volume ratio). Crystal information was collected by EBSD device. The evolution of cementite, dislocation and substructure was characterized by TEM (Tecnai G2F20 system, operated at 200 kV). The TEM sample was grinded to 30 to 50 μm with metallographic sandpaper and stamped into ϕ 3 mm wafers, followed by double-jet electrolytic thinning of electrolyte (the same as the polishing solution). Image Pro Plus was used for microstructure statistical analysis, and MATLAB was used for data fitting.

The dog bone tensile samples with a standard distance of 10 mm and width of 5 mm were cut along the rolling direction. The uniaxial tensile test was carried out by Instron electronic universal testing machine to evaluate the tensile properties of the annealed samples. The strain rate is  $5 \times 10^{-4} \text{ s}^{-1}$ . In order to ensure data repeatability, at least three independent samples were measured repeatedly for each type of sample.

### III. EXPERIMENTAL RESULTS

#### A. Microstructure Characterization

Figure 1(a) is the initial structure of plain medium carbon steel consisting of 43.1 pct ferrite. The pseudo-eutectic structure of plain medium carbon steel is obtained by quenching in water at 90 °C as shown in Figure 1(b). After the hot-water quenching, the content of primary ferrite is significantly reduced to only 11 pct, while the interlayer spacing of cementite layers is finer and the content of pearlite is higher. The particular structure of the distribution of primary ferrite at grain boundaries is a key factor in the subsequent warm rolling to form a lamellar structure.

Figure 2 is the SEM photos of the microstructure after warm deformation and annealing at 600 °C for 30 minutes. The lamellar structure of the sample was not obvious at 80 pct deformation. The proeutectoid ferrite was elongated along the rolling direction. The pearlite lamellar structure was partially destroyed, and a certain volume fraction of the ferrite + cementite lamellar structure was retained. Compared with the sample deformed to 80%, the lamellar structure with deformation of 84 pct was more obvious, and the proeutectoid ferrite was further elongated and flattened along the rolling direction. The cementite was twisted and broken, and the grain rotation occurs under large strain. When the deformation increased to 88 pct, the proeutectoid ferrite showed a clear banded structure and the thickness became thinner, and the spheroidization degree of cementite further increasing. After annealing, the cementite spheroidized and the initial pearlite lamellae completely disappeared. A part of primary ferrite (proeutectoid ferrite) structures only recovered without recrystallization, forming subgrains. The ferrite grain boundaries in the initial pearlite area were pinned by cementite, so the grain size after recrystallization was fine. The intercrystalline cementite was obviously coarsened because of the high concentration of dislocations or vacancies after warm rolling, the carbon atoms diffused to the low carbon concentration region (proeutectoid ferrite) and then precipitate at the most favorable energy position (grain boundary/triple junction).

The fine intragranular cementite was caused by low density dislocation/vacancy. With the increase of deformation, the intercrystalline cementite after annealing had a tendency of coarsening.

Figure 3 shows EBSD image of warm rolled samples annealed at 600 °C for 30 minutes. A heterogeneous lamellar structure was still maintained after annealing of warm rolled samples with different deformations. Figures 3(a) and (b) show that there are few banded deformed coarse grains in the annealed microstructure with deformation of 80 pct, and most of the recrystallized grains are equiaxed. The annealing microstructure with deformation of 84 pct was characterized by alternating arrangement of thin ferrite sheets, which was due to the recovery and incomplete recrystallization of the ANWR84, resulting in the retention of the deformed lamellar ferrite structure after rolling to some extent. The microstructure of ANWR88 was characterized by coarse ferrite bands surrounded by equiaxed UFG. There are two factors that may form coarse lamellar ferrite. One is that the severely deformed ferrite lamella recrystallizes and gathers into thicker ferrite lamella. Second, the deformed ferrite grains fully recrystallized and grown. When the warm rolling deformation is larger, the defects of internal deformation and stored deformation energy are higher and the stability in the annealing process is relatively weakened. The structural defects are conducive to the nucleation of the recrystallization process, and the stored energy is transformed into the driving force of grain growth in the recrystallization process. Therefore, the greater the deformation, the lower the recrystallization temperature, and the more complete the return recrystallization under the same annealing conditions (temperature, holding time).

Figure 4 is the statistical result of grain diameter of annealed samples. The ferrite grain sizes of ANWR80, ANWR84 and ANWR88 are 0.66  $\mu\text{m}$ , 0.63  $\mu\text{m}$  and 0.76  $\mu\text{m}$  respectively. Furthermore, the cementite after annealing is reported to be smaller than that after warm rolling, and the cementite particles are fine and dispersed.<sup>[20]</sup> It can be seen from Figure 4(d) that when the ANWR80, ANWR84 and ANWR88 were annealed for 30 minutes, the proportions of small angle grain

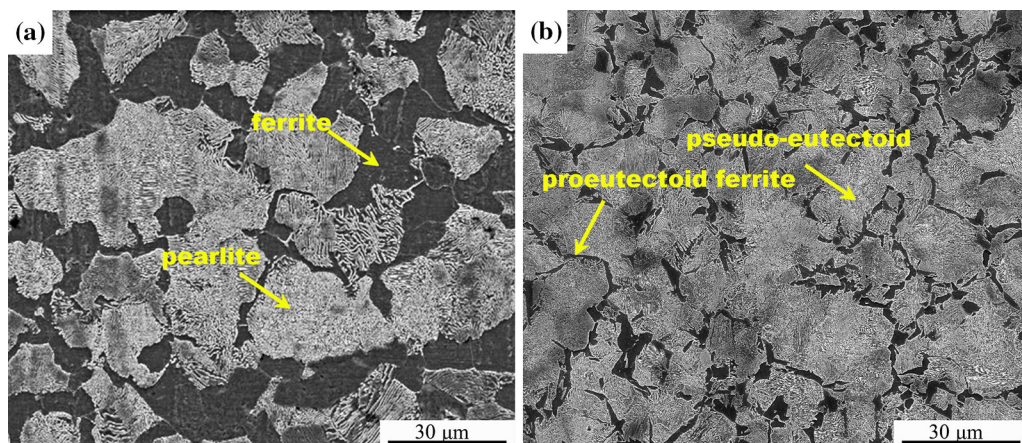


Fig. 1—Micrographs of (a) the microstructure of plain medium carbon steel, (b) after quenching the pseudo-eutectoid structure.

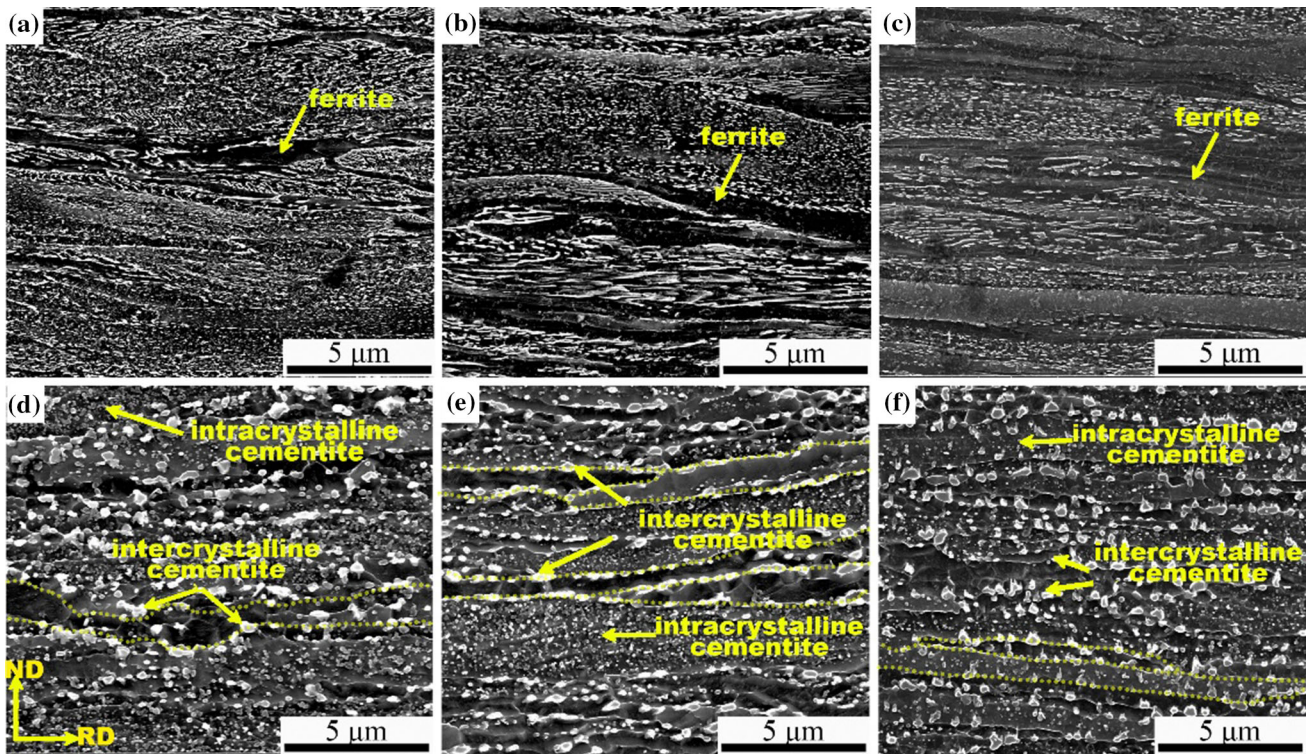


Fig. 2—SEM microstructure of rolled and annealed samples: deformations of rolled samples are (a) 80%, (b) 84%, (c) 88%, annealed samples (d) ANWR80, (e) ANWR84, (f) ANWR88.

boundaries of the corresponding experimental steel are 49.2, 46.4 and 45.4 pct respectively. And the corresponding proportions of large angle grain boundaries are 50.8, 53.6 and 54.6 pct respectively. When the deformation further increases to 88%, the proportion of small angle grain boundaries corresponding to the annealed sample decreases. In the annealing process, the subgrain boundaries continuously absorb the internal dislocations and increase the thickness of the subgrain boundaries, resulting in the increase of the orientation angle difference between the subgrains, and finally form the large angle grain boundaries, thus increasing the proportion of the large angle grain boundaries.

The ferrite matrix of annealed samples with different deformation has a typical heterogeneous structure distribution, forming a cross-scale grain distribution. The grain size of the experimental steel can be divided into three grain levels, namely, ultra-fine grains (UFG:  $d \leq 1 \mu\text{m}$ ), fine grains (FG:  $1 \mu\text{m} < d \leq 5 \mu\text{m}$ ) and coarse grains (CG:  $d > 5 \mu\text{m}$ ), and the grain size is in the range of nanometer to micrometer. The obvious cross-scale grain grade leads to sharp mechanical incompatibility and strain gradient on heterogeneous interfaces during plastic deformation. Thus, the hetero-deformation induced hardening (HDI hardening) peculiar to heterogeneous structures is generated. Combined with the homogeneous structure of the forest dislocation strengthening effect, the synergistic effect of strength and plasticity is improved. The statistics of area fraction changes of grain sizes of different grades in warm rolling and annealing samples are shown in Table I.

Figure 5 shows the grain orientation spread (GOS) distribution of annealed samples, and the dynamic recrystallization degrees of ANWR80, ANWR84 and ANWR88 are 75, 94 and 98 pct respectively. Therefore, there were a large number of equiaxed UFG in the ANWR80, which refined the coarse ferrite deformation layer. The partial recrystallization degree of ANWR84 is higher than that of ANWR80, so the degree of grain refinement is further increased than that of ANWR80. The increase of deformation provides a driving force for the precipitation of a large number of nano-scale cementite particles inside the ferrite. The cementite at the grain boundaries was further spheroidized and slightly coarsened compared with the ANWR80, and its distribution inhibits the pinning degree of ferrite growth, so its grain size was finer than that of the ANWR80. Considering that the ANWR88 was almost completely recrystallized, the grain growth of dynamic recrystallization in the shear band produced by warm deformation is restrained by the cementite particles at the grain boundaries. At the same time, the grain growth rate of the ferrite recovery was significantly accelerated, and the large deformation amount provided a driving force for grain growth. Therefore, the lamellar microstructure was coarsening and the grain size is larger than that of the warm rolled ANWR84.

Figure 6 shows TEM photographs of different annealed samples. It can be seen that with the increase of deformation, the morphology of cementite in the sample gradually spheroidized into discontinuous short rods, and the size gradually decreased. The coarser cementite particles precipitate at the ferrite grain

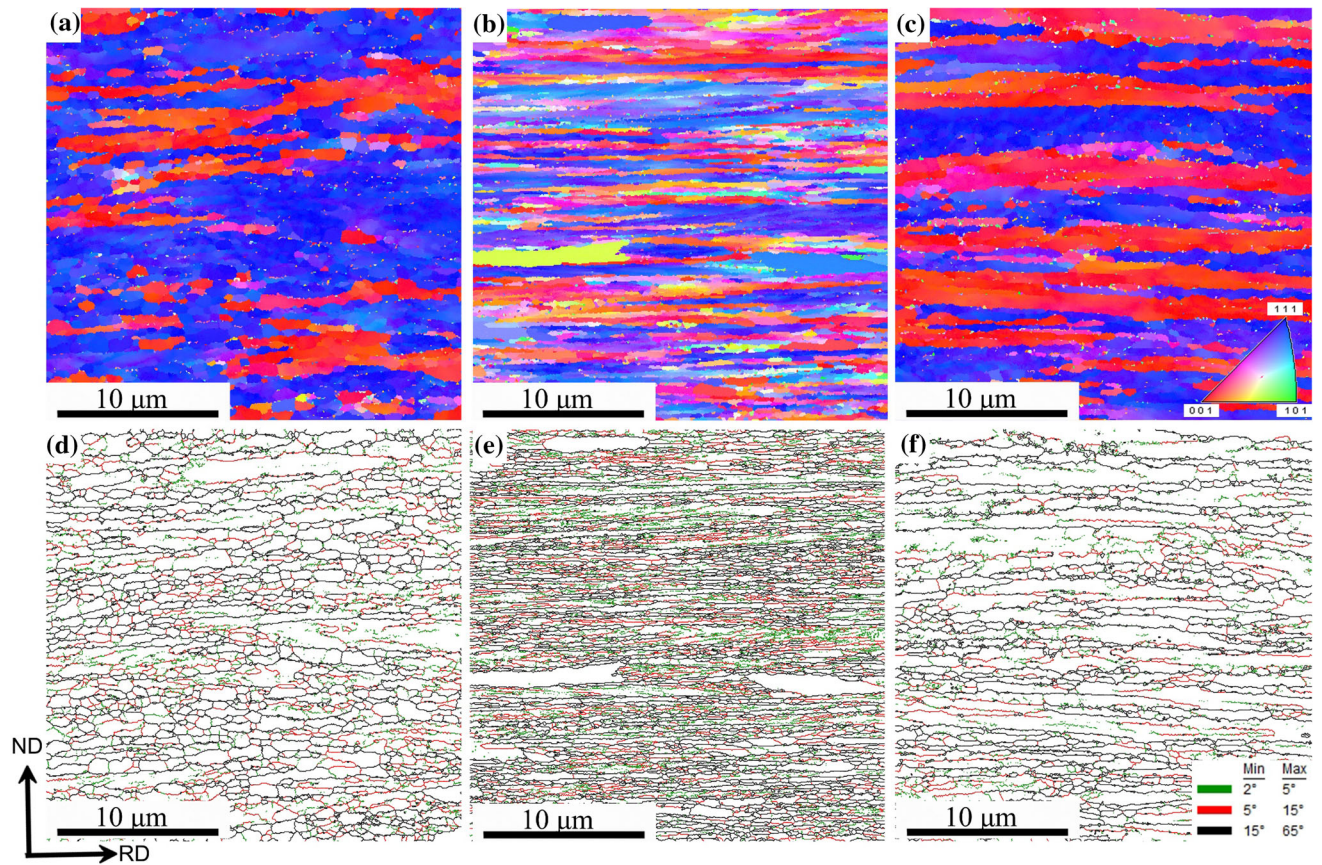


Fig. 3—EBSD photographs of annealed samples: (a) and (d) ANWR80, (b) and (e) ANWR84, (c) and (f) ANWR88. The green corresponds to subgrain boundary  $2 \text{ deg} \leq \theta \leq 5 \text{ deg}$ ; red represents small angle grain boundary  $5 \text{ deg} \leq \theta \leq 15 \text{ deg}$ ; blue represents large angle grain boundary  $\theta \geq 15 \text{ deg}$  (Color figure online).

boundaries and triple junctions, and finer cementite precipitate at the ferrite grain interiors. It is due to the favorable nucleation of carbon trapped within the ferrite grains, resulting in finer cementite grains. The nucleation of cementite particles at grain boundaries and triple junctions is larger than that within the grain boundaries due to the faster diffusion of carbon atoms at the grain boundaries.<sup>[21]</sup>

There were high density dislocations in ANWR80 and ANWR84. These dislocations were intertwined and intersected, forming several cellular substructures near the phase boundaries. More geometrically necessary boundaries (GNBs) remained near grain boundaries.<sup>[22,23]</sup> At the same time, a large number of vertically or mutually incidental dislocation boundaries (IDBs) remained between GNBs<sup>[22,23]</sup> Compared with the ANWR80, the IDBs region of the ANWR84 is significantly reduced, the substructure boundaries were gradually clarified, and a small number of dislocations exist in the recrystallized grains. The IDBs were almost not observed in the ANWR88, the dislocation density was greatly reduced and the degree of recrystallization was

further improved. The Figure 6 shows that as the deformation increases, the number of grains with dislocation structures decreases. The dislocation entanglement of the annealed sample becomes more and more obvious (red circles), finally the dislocations aggregate to form dislocation cells, forming subgrains.

#### B. Mechanical Behaviors of Warm-Rolled Plain Medium Carbon Steel after Annealing

Figure 7 shows the engineering stress–strain curves of the annealed samples at room temperature. Table II shows the specific mechanical properties of the samples. It can be seen that Lüders band appears during the tensile deformation, and the contributions of Lüders band on the elongation of ANWR80, ANWR84 and ANWR88 are 1.3, 1.7 and 3.4 pct respectively, which is mainly because of cementite. After annealing, the cementite became finer, more uniform and the density tended to decrease with deformation increasing. The volume fraction of cementite decreased (according to Figure 4; Table III), demonstrating that the solubility of

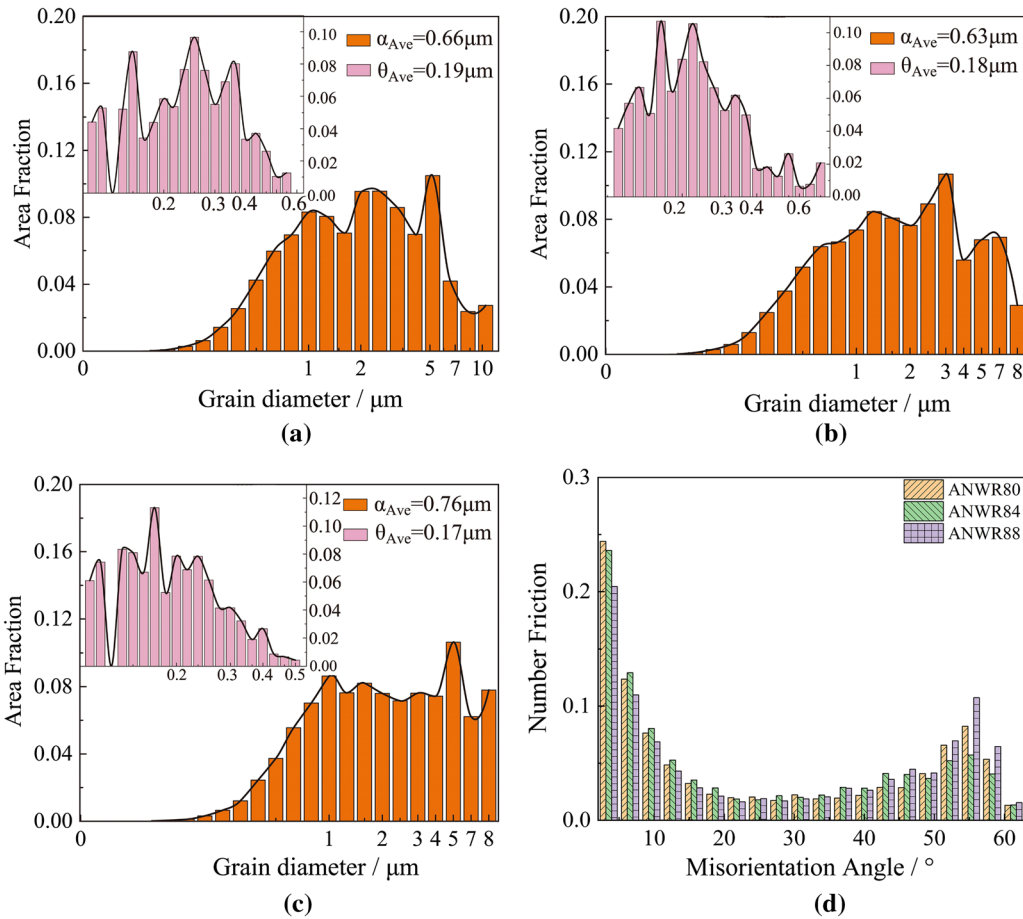


Fig. 4—The proportions of grain size and cementite size of annealed samples (a) ANWR80, (b) ANWR84, (c) ANWR88 and (d) proportion of grain boundaries angle.

**Table I. Area Fraction of Heterogeneous Grain Lamellar of Annealed Samples**

Samples	UFG (Pct)	FG (Pct)	CG (Pct)
ANWR80	22	58	20
ANWR84	26	57	17
ANWR88	21	54	25

carbon atoms in ferrite increased. During the tensile process, the dislocations were pinned by carbon atoms, the greater the probability of the formation of Cottrell atmosphere, resulting in more stress fluctuations. The stress-strain curve was characterized by stress fluctuation, and each fluctuation was equivalent to the formation of a new Lüders band. The toughness is a comprehensive parameter including strength and uniform plasticity, and its value is the product of tensile strength  $\sigma_b$  and uniform elongation  $\varepsilon_u$ . The toughness values of ANWR80, ANWR84 and ANWR88 are 6898, 7002 and 6018 MPa pct respectively. For ANWR84 with obvious ultrafine grain and lamellar structure, the yield strength reaches 751 MPa, while its uniform elongation is still 9%, showing good service performance.

## IV. DISCUSSION

### A. Strengthening Mechanism of Heterogeneous Lamellar Structure Plain Medium Carbon steel

Compared with the tensile strength of the experimental steels after annealing, the tensile strengths of the ANWR80, ANWR84 and ANWR88 are 737, 778 and 725 MPa respectively. The ANWR84 showed the highest strength, which may be related to the proportion of each grain lamellar and the dislocation density of the annealed sample. In the heterogeneous microstructure composed of CG and UFG regions, the strain distribution during deformation requires the existence of the geometrically necessary dislocation (GND) to maintain the compatibility of interfaces with different grain grades. Figure 8 shows the statistical distribution of GND density of warm-rolled samples based on kernel average misorientation (KAM) data. The GND density  $\rho^{\text{GND}}$  of the annealed samples can be obtained by the KAM value (ignore the statistical dislocation)<sup>[24,25]</sup>:

$$\rho^{\text{GND}} = \frac{2\Delta\theta_i}{ub} = \frac{2\theta_{\text{agv}}}{ub} \quad [1]$$

where  $b$  is Burg vector (0.248 nm);  $\mu$  is EBSD scan step (60 nm),  $\theta_{\text{agv}}$  is average of KAM.

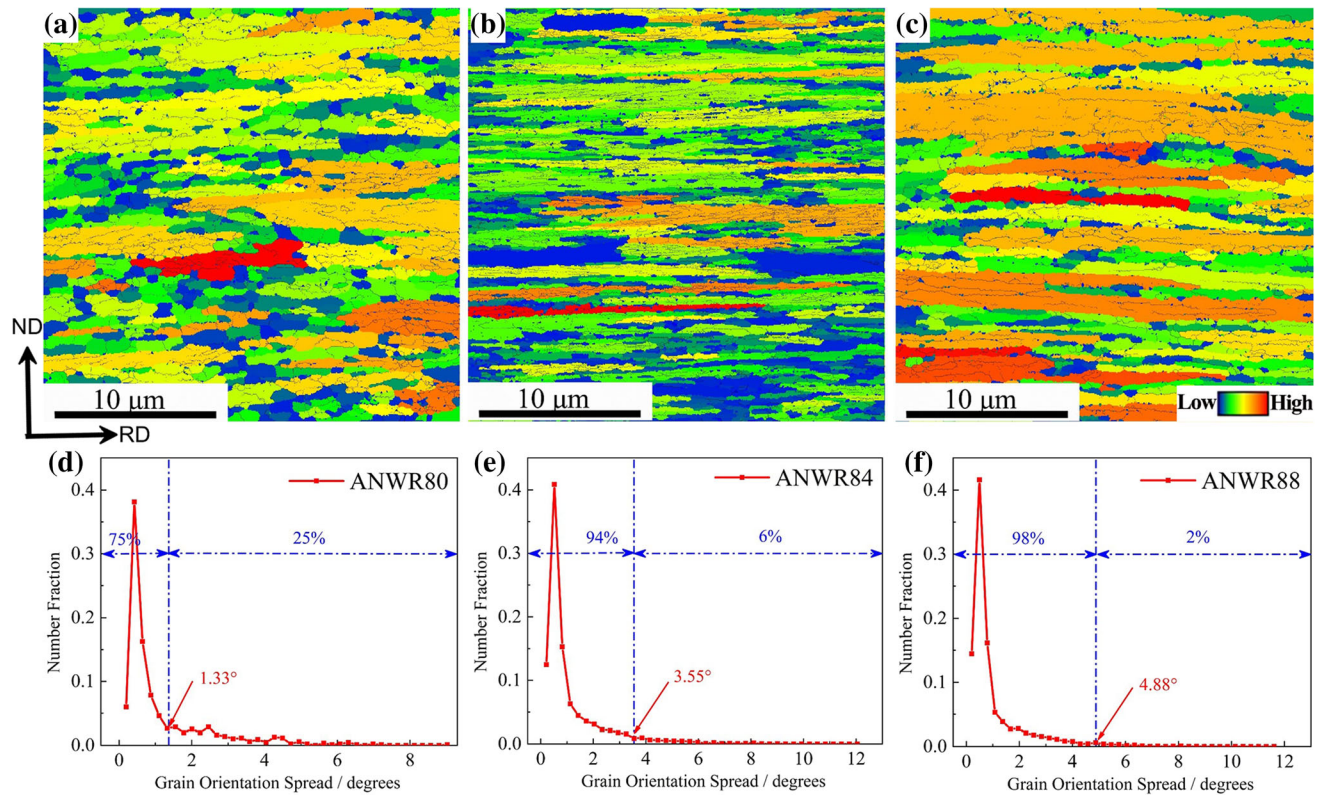


Fig. 5—The GOS distribution and GOS numerical statistics of annealed samples: (a) and (d) ANWR80, (b) and (e) ANWR84, (c) and (f) ANWR88 (In the rainbow legends, blue to red represents an increase in GOS values.) (Color figure online).

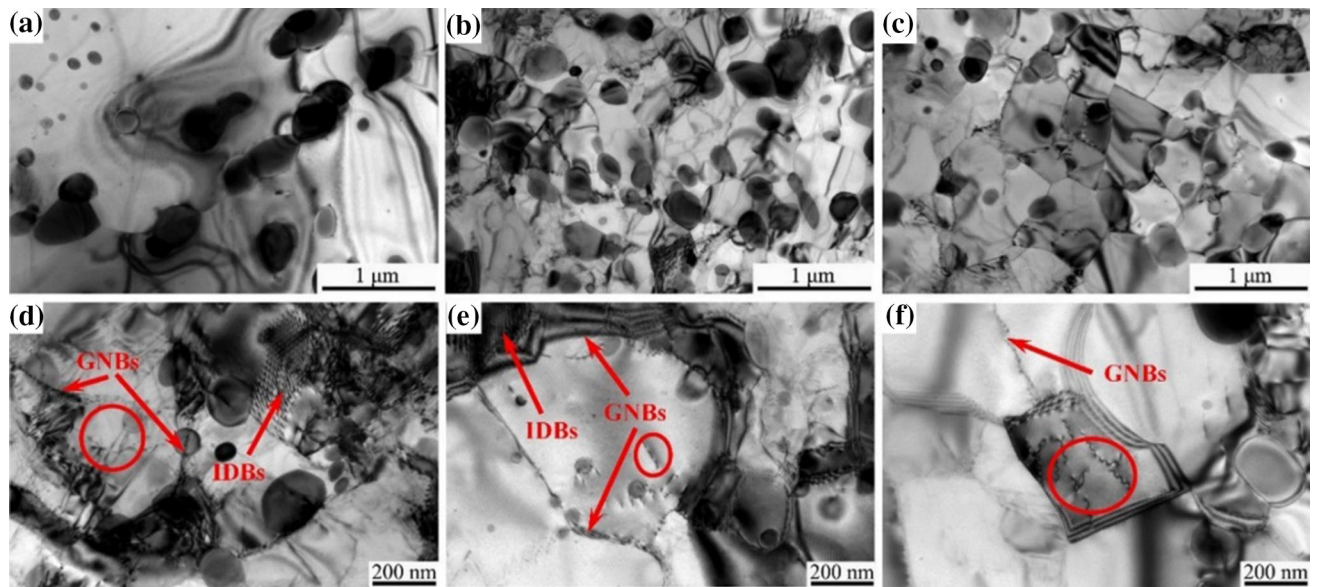


Fig. 6—The TEM photographs of annealed samples: (a) and (d) ANWR80, (b) and (e) ANWR84, (c) and (f) ANWR88.

Therefore, the dislocation strengthening increment can be calculated:

$$\sigma_{\text{dis}} = \alpha M G b \sqrt{\rho^{\text{GND}}} \quad [2]$$

where  $\alpha$  is constant,  $\sim 0.1$ ,  $M$  is Taylor factor,  $G$  is shear modulus (80 GPa).

Combined with the equation, the ANWR84 had the highest GND density, which leads to the highest strengthening caused by the back stress. After annealing, the dislocation annihilation in the microstructure of the samples makes the dislocation density significantly lower. More dislocations can be accommodated inside the grains, so the elongation of the samples is higher



after annealing. As shown in Figures 5(d) through (f), the GOS recrystallization of the annealed samples shows that the ANWR80 is incompletely recrystallized and has a minimum recrystallization of 75 pct. Mechanically driven nanocrystalline growth occurs under plastic deformation, which could partially restore the dislocation plasticity of UFG. Yang<sup>[26]</sup> and Jiang<sup>[27]</sup> found that the forest dislocations were the main reason for good elongation. The forest dislocations occur within dislocation boundaries and specifically in two types of boundaries: IDBs and GNBs<sup>[22]</sup> (shown in Figure 6). The elongation of ANWR88 is the lowest due to the lowest forest dislocations. ANWR80 and ANWR84 have similar forest dislocations, but ANWR80 has higher FGs and CGs ratios. Therefore, the effective forest dislocation hardening made the ANWR80 exhibit the highest elongation.

A large number of spheroidized cementite dispersed in the microstructure of annealed samples. The experimental steels showed the heterogeneous characteristics of bimodal distribution of second phase. Considering the heterogeneous lamellar distribution of the ferrite matrix, the characteristics of experimental steels were double heterogeneous structure. During the annealing process, a large number of dispersed nano-cementite precipitate in grains. Studies have shown that for nanoparticles, the increment of dislocation strengthening can be considered as the contribution of yield strength caused by dislocation cutting nanoparticles. In other words, the strength increases from the precipitation strengthening

of intragranular cementite was calculated based on Orowan mechanism,  $\sigma_{ig}$  can be given by the relationship of Eq. [3] [28]:

$$\sigma_{ig} = \frac{0.7MGb\sqrt{f_{ig}}}{d_{ig}} \quad [3]$$

where  $f_{ig}$  is volume fraction of the intragranular cementite,  $d_{ig}$  is average size of intragranular cementite.

The contribution of intercrystalline cementite to strength was limited, and even when the coarse cementite particles are located at the grain boundaries, stress concentration will lead to the early fracture of the sample. The contribution of intergranular coarse cementite to yield strength can be calculated by dispersed barrier hardening model, the following equation<sup>[29]</sup>:

$$\sigma_{gb} = M\alpha Gb\sqrt{\rho_{gb}d_{gb}} \quad [4]$$

where  $\alpha$  is the barrier strength factor,  $\rho$  is the density, and  $d$  is average size of intergranular cementite.

The size, volume fraction and density-related information of the cementite are counted by multiple microstructure images, and the results are shown in Table III. Due to the uneven size of the cementite, the ROM calculation method is used to calculate the cementite strengthening value of the sample.

Therefore, the effective grain boundaries strengthening represented by Hall–Petch rewriting can be expressed as:

$$\sigma_{GB}^* = k_y \times d^{-\frac{1}{2}} \quad [5]$$

According to Table I, the calculated grain boundary strengthening values of each annealed sample are shown in Table IV by ROM calculation method.

The strengthening mechanism of annealed experimental steels includes Pile's stress, intergranular particle strengthening, dispersion solid solution strengthening and grain boundaries strengthening through the following equation:

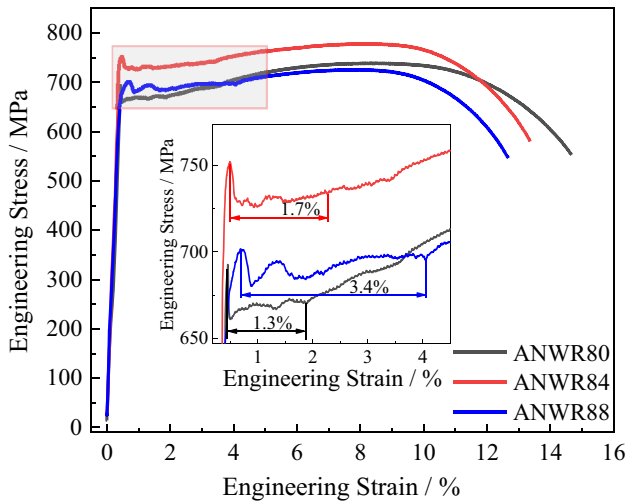


Fig. 7—The stress–strain curves of annealed samples.

Table II. The Mechanical Properties of Annealed Samples

Samples	$\sigma_{YS}$ (MPa)	$\sigma_b$ (MPa)	$\epsilon_u$ (Pct)	$\epsilon_t$ (Pct)	Toughness (MPa Pct)
ANWR80	691	737	9.36	14.7	6898
ANWR84	751	778	9	13.4	7002
ANWR88	700	725	8.3	12.6	6018

Table III. The Volume Fraction of Cementite Particle Size of Annealed Samples

Samples	$\rho_{gb}$ (m <sup>-3</sup> )	$f_{gb}$	$f_{ig}$	$d_{gb}$ (nm)	$d_{ig}$ (nm)
ANWR80	$6.2 \times 10^{17}$	0.20	0.15	200	178
ANWR84	$5.1 \times 10^{17}$	0.17	0.21	230	155
ANWR88	$5.1 \times 10^{17}$	0.13	0.27	260	130

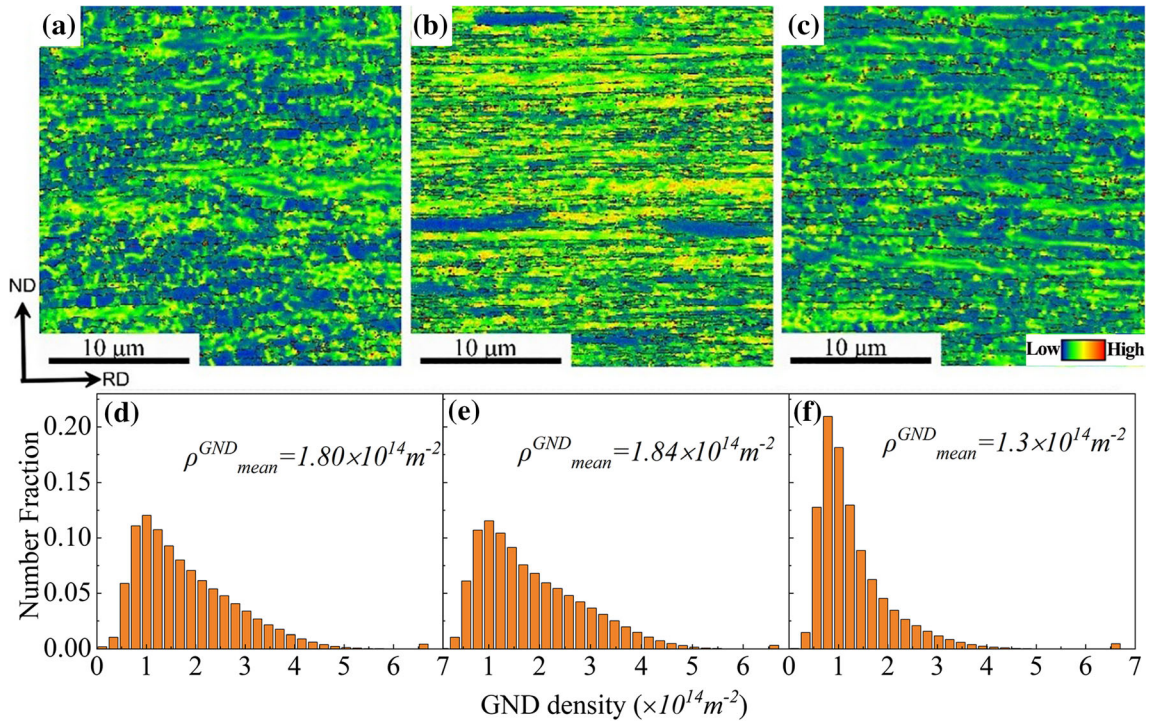


Fig. 8—The KAM and GND density distribution of annealed samples: (a) and (d) ANWR80, (b) and (e) ANWR84, (c) and (f) ANWR88 (In the rainbow legends, blue to red represents an increase in KAM values.) (Color figure online).

$$\sigma_{YS} = \sigma_0 + \sigma_s + \sigma_{dis} + \sigma_{GB}^* + \sigma_p + \sigma_{Oworn} \quad [6]$$

The calculation results of strengthening increment caused by various strengthening mechanisms of annealing experimental steel are summarized in Table V.

Figure 9 shows the comparison of the strengthening mechanism with the calculated and actual values. The actual values of the experimental steel are higher than the theoretical calculation values, and there are similar reports.<sup>[30,31]</sup> There is an additional strengthening mechanism in heterogeneous structure experimental steel, namely the HDI strengthening mechanism. It can cooperate with other strengthening mechanisms to increase elongation while maintain strength. The ANWR84 sample showed a higher additional strengthening increment than other samples with different deformations. Considering the extra strengthening of heterogeneous structure, the grain structure of the ANWR84 was reasonable (the highest proportion of UFG). Combined with the experimental results, the ANWR84 showed the highest toughness, the synergistic effect of strength and plasticity was the best. During plastic deformation, the CGs lamellae yield initially, while most UFGs remain elastic. A large amount of dislocation accumulation in the thicker lamellae, which leads to higher shear stresses and reaches the critical shear stress earlier. Therefore, in the subsequent deformation, CGs sustain greater plastic strain than FGs. According to the proportion of grain level (Table I), the ANWR84 has the largest difference between UFG and CG, which leads to a higher plastic strain gradient, so

that the HDI substantially increases the tensile strength of the experimental steel. This indicates that the grain distribution of UFG, FG and CG with ANWR84 is the most optimal.

For the plain medium carbon steel in this study, it has a good uniform elongation while maintaining high yield strength, and has better deformation and failure resistance in the same grade of micro alloyed steel.<sup>[32–34]</sup> Therefore, plain medium carbon steel with heterogeneous laminate structure has a good application prospect in the structure with high strength and good stability.

### B. Strain Hardening Behavior of Heterogeneous Lamellar Plain Medium Carbon Steel

Figure 10 shows the variation of the fraction of M value calculated by Taylor Factor (TF) under grain boundaries conditions through EBSD data. The TF of M values between 4 and 5 of ANWR80, ANWR84 and ANWR88 are 24, 12 and 9 pct, respectively. Taylor<sup>[35]</sup> introduced the concept of deformation of crystals by dislocation slip and formulated the relationship between shear flow stress  $\tau$  and the dislocation density  $\rho$  ( $\tau = \beta G b \sqrt{\rho}$ ). The shear flow stress is positively correlated with M value. According to Hansen's research<sup>[36]</sup>,  $\beta$  usually decreases as GND increases. The reason for the highest M of sample ANWR80 was that the higher dislocation density and a lower  $\beta$ . The average TF values of ANWR80, ANWR84 and ANWR88 are 3.49, 3.41 and 3.24, respectively. The higher the average TF value was, the harder the sample slides in deformation and yielding at low stresses deformed. The

**Table IV. The Grain Boundaries Strengthening Increment of Heterogeneous Grain Laminate Structure After Annealing**

Samples	UFG (MPa)	FG (MPa)	CG (MPa)	$\sigma_{GB}^*$ (MPa)
ANWR80	128	155	36	319
ANWR84	146	153	28	327
ANWR88	123	135	44	302

**Table V. Contributions of Strengthening Mechanisms of Annealing Samples**

Samples	$\sigma_{gb}$ (MPa)	$\sigma_{ig}$ (MPa)	$\sigma_{dis}$ (MPa)	$\sigma_{GB}^*$ (MPa)	$\sigma_{YS}$ calculated (MPa)	$\sigma_{YS}$ test (MPa)
ANWR80	76	65	93	319	654	691
ANWR84	74	86	92	327	680	751
ANWR88	78	116	73	302	670	700

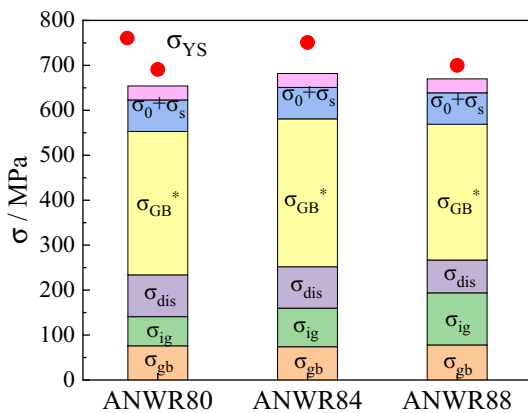


Fig. 9—Comparison chart of each strengthening increment of samples.

strain-hardening first appears inside the larger size laminated ferrite grains. The non-uniformity of the activation system drives the TF deformation of ferrite orientation rotation. To coordinate the deformation, dislocations near the boundaries interact. The dislocations either obliterate or slip into the ferrite internal, thus deforming the interface.

The higher average M values imply higher strain hardening rate (SHR) peaks for the samples (Figure 11(a)), and thus the SHR peaks for ANWR80, ANWR84, and ANWR88 are sequentially lower. As mentioned in many reports,<sup>[37–39]</sup> the low peak SHR makes the material poorly resistant to deformation after yielding and limits its ability to resist accidental overloads during service.

The microstructure of ANWR80 has less lamellar structure and more equiaxed grains. The ANWR84 and ANWR88 showed similar characteristics of alternating distribution of ferrite sheets with different thicknesses. Figure 11 shows the strain hardening rate curve and the relationship between instantaneous strain  $n$  and true strain of the samples.<sup>[40]</sup> The SHR peak of ANWR84 is higher than that of ANWR88, and a higher peak means stronger strain hardening ability. The earliest strain hardening stage of ANWR80 was related to the Lüders

band in the sample. The essence of strain hardening in the rapid proliferation of dislocations increased with the increase of strain. Then the interaction between dislocations became stronger, resulting in the increase of the resistance of dislocation motion. In the contrast, for precipitation-reinforced alloys, strain hardening is mainly related to blocked dislocation motion caused by dislocation–dislocation and dislocation-particle interactions.<sup>[41,42]</sup> The high-density dislocation is beneficial to improve the SHR of the alloy through the effect of the interface effect (phase interface/ grain boundary) of forest dislocation.<sup>[26,27]</sup> The dislocation density of ANWR88 is the lowest, showing the lowest SHR. Under uniaxial stress, the strain hardening ability of the alloy was positively correlated with the shear flow stress  $\tau$ , that is, the SHR value was positively correlated with the TF value.

As can be seen from Figure 11(b), the  $n$ -value rises in a fluctuating state until it reaches the maximum value. And the  $n$ -value of ANWR80 is the highest and decreases rapidly after reaching the maximum value, which may be due to the fact that the microstructure is mainly composed of FG and UFG. In the ANWR84 and ANWR88, after the  $n$  value reaches the maximum, it fluctuates within a range, which is caused by the uniform deformation of the heterostructure during the deformation process. During the tensile process, as the large size lamellar grains began to deform plastically the UFG still maintains elastic deformation, showing mechanical incompatibility. Figure 12 shows the KAM diagram, GND diagram and point-to-point diagram of CGs and the surrounding fine grains. Most UFGs and FG have high KAM and GND values. According to the curves of point-to-point map, the fluctuation of KAM and GND values are similar, but the changes of GND values have certain hysteresis. The Lin1 shows that the Kam value and GND value reach the highest near the grain boundaries, as shown by the arrow in Figure 12(c). Under the action of stress, the high GND value near the grain boundaries make the CGs unable to deform freely, so the strain gradient appears near the boundaries of the large grains. During the continuous increase of strain, the GND continuously

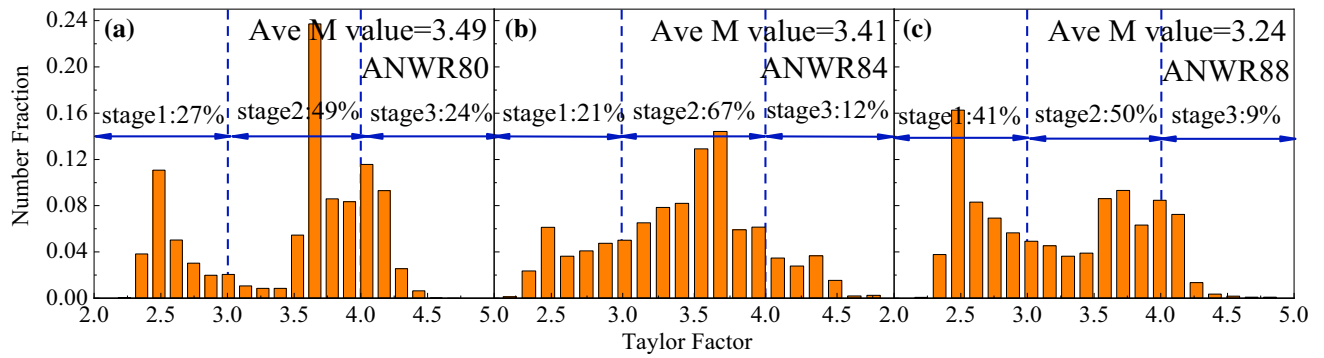


Fig. 10—The TF diagram of annealing samples: (a) ANWR80, (b) ANWR84, (c) ANWR88.

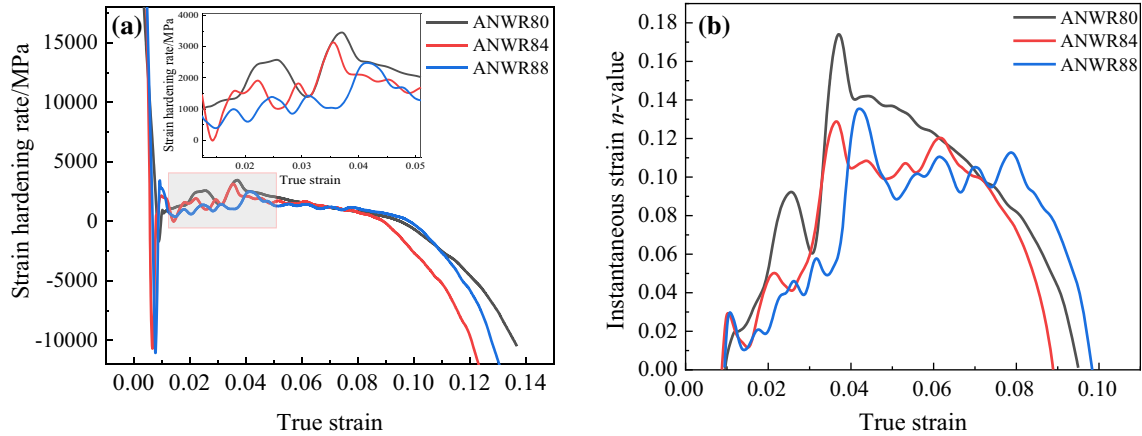


Fig. 11—(a) The strain hardening rate variation curve and (b) strain hardening index curve.

accumulates near the grain boundaries, and the back stress gradually increases to adapt to the strain gradient and maintain the deformation compatibility between the CG and the FG. The GND value also fluctuates in the CGs, such as Lin2. Therefore, when the dislocation moves to the inside of the grain, the resistance is not uniform, resulting in stress fluctuations. The transient fluctuation of  $n$ -value is caused by the synergistic deformation between CGs and FGs and the uneven distribution of GND in the CGs.

The flow stress model of materials refers to the functional model used to describe the corresponding relationship between the true stress  $\sigma$  and the true strain  $\varepsilon$  of materials. Fitting analysis was carried out for the ANWR84 with a heterogeneous lamellar structure. There are a variety of flow stress models, and different models have different fitting errors for the flow stress curves. Therefore, a comparative analysis of the fitting effect of different flow stress models on the test curves was needed. The plastic strain flow stress model is generally expressed as  $\sigma = \sigma(\varepsilon_p)$ , where  $\varepsilon_p$  is true strain. The following plastic strain flow stress models were selected: the Ludwik,<sup>[43]</sup> Swift,<sup>[44]</sup> Samanta,<sup>[45]</sup> Voce-Kocks,<sup>[46,47]</sup> and Misiolek.<sup>[48]</sup>

The plastic flow stress model was used to fit the partial true strain curve ( $> 0.01$ ) after yielding. The plastic strain flow stress model was fitted using the nonlinear

fitting tool of MATLAB software, and the obtained fitting results are shown in Table VI and Figure 13. In terms of the root mean square error and the curve fitting effect, the fitting effect of the four models is still satisfactory except for the Samanta model. The true stress-true plastic strain curves of plain medium carbon steel after the yield plateau were accurately described. The main differences between the fitted curves of the four models are in the fitting of the starting and ending segments of the curve. From Figure 13, it can be seen that the fitted curves of the Voce-Kocks model are closer to the real test curves than those of the Ludwik, Swift, and Misiolek model. The starting point of the curve is closer to the real test curve, so the fitted results of the Voce-Kocks model are used to model the flow stress of plain medium carbon steel after the yield platform. After verifying, Voce-Kocks is still accurate in fitting the true stress-true strain curve of ANWR88. This shows that the Voce-Kocks model can accurately describe the functional relationship between stress and strain of plain medium carbon steel with a heterogeneous lamellar structure. It was verified that the Voce-Kocks model was still accurate in fitting the true stress-true strain curves of the ANWR88. It showed that the Voce-Kocks model can be more accurate as a function of stress and strain for the heterogeneous laminar plain medium carbon steel.

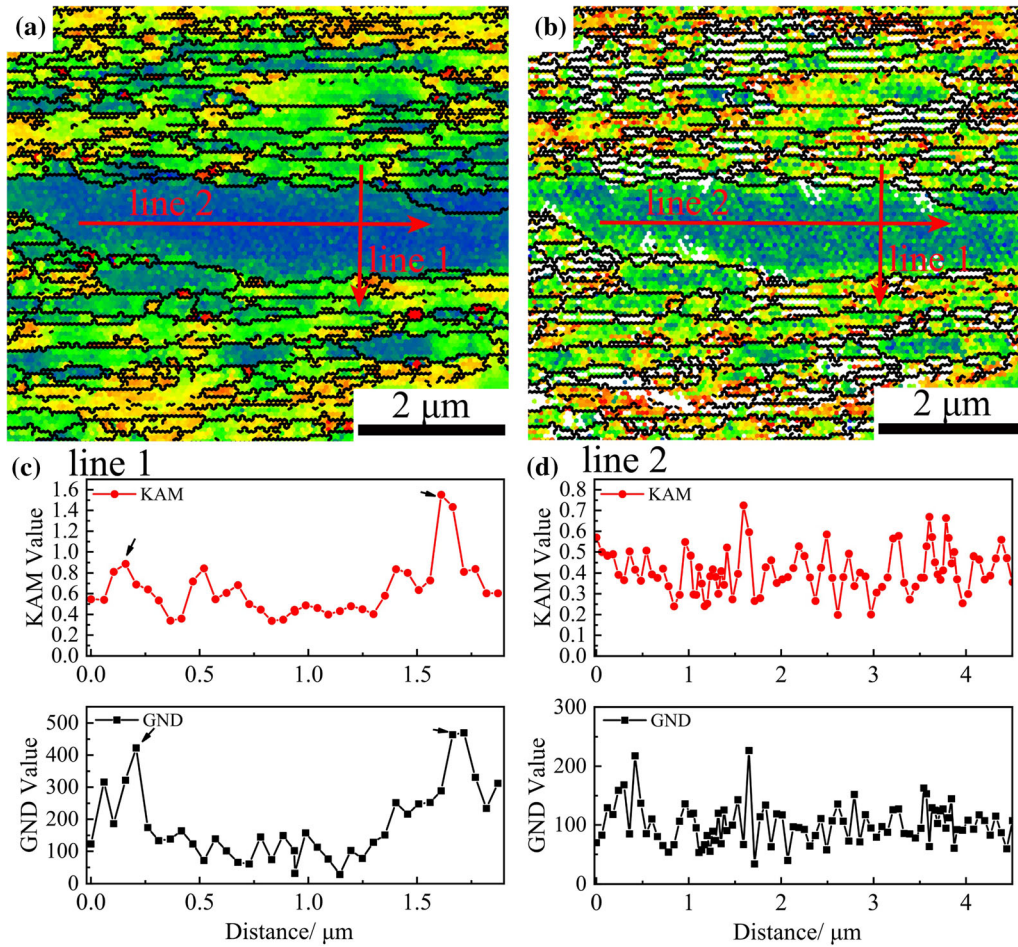


Fig. 12—The (a) KAM map, (b) GND map and (c), (d) corresponding point-to-point maps.

Table VI. Comparison of Fitting Effects of Different Flow Stress Models

Models	Material Parameters	Parameters
Ludwik: $\sigma = \sigma_0 + A \cdot \varepsilon_p^n$	$\sigma_0 = 693.1, A = 993.9, n = 0.74$	R-square: 0.9995, RMSE: 0.9875
Swift: $\sigma = A \cdot (\varepsilon_p + \varepsilon_0)^n$	$A = 1280, \varepsilon_0 = 0.051, n = 0.20$	R-square: 0.9997, RMSE: 0.772
Samanta: $\sigma = \sigma_0 + A \cdot \ln \varepsilon_p$	$\sigma_0 = 1057, A = 84.74$	R-square: 0.9996, RMSE: 0.9339
Voce-Kocks: $\sigma = \sigma_s - (\sigma_s - \sigma_0) \cdot e^{-n \cdot \varepsilon_p}$	$\sigma_s = 956, \sigma_0 = 700, n = 10.12$	R-square: 0.9998, RMSE: 0.6821
Misiolek: $\sigma = A \cdot \varepsilon_p^n \cdot e^{n_1 \cdot \varepsilon_p}$	$A = 806.5, n = 0.026, n_1 = 1.46$	R-square: 0.9992, RMSE: 1.035

*R-square* Coefficient of determination, *RMSE* Root mean squared error.

## V. CONCLUSIONS

In this study, a proposed method for establishment of multiscale lamellar structure based on plain medium carbon steel is presented. First, a pseudo-eutectoid microstructure with intermittent strip distribution of ferrite along the pearlite grain boundaries was obtained by pretreatment. Subsequently, the size and distribution of ferrite heterogeneous lamellar microstructure and cementite are regulated by warm rolling (80/84/88 pct) and short annealing (600 °C/30 minutes). High strength

and elongation were obtained for plain medium carbon steel, and the mechanical properties of low-alloy high-strength steel were achieved.

1. The cross-scale heterogeneous lamellar structure embedded with UFG was formed after warm rolling annealing. With the increase of deformation, the recrystallization ratio gradually increases after annealing, the IDB gradually decreases, the GND value first increases and then decreases, and the grain size first decreases and then increases. The

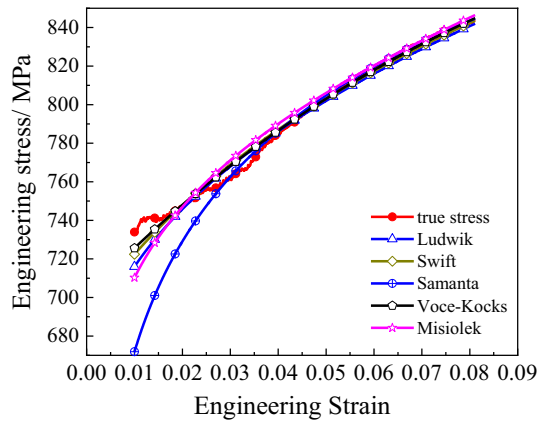


Fig. 13—Comparison of fitting curves of different flow stress models.

- annealed samples with 84% deformation have the best ratio of UFGs, FGs and CGs. The highest density of gradient-distributed GNDs accumulated at the interface of the soft domains was exhibited, contributing to the HDI mechanism and providing additional strength and plasticity. Thus, 84% of the annealed samples have high strength and plasticity.
- The spheroidization of cementite occurs in the samples annealed at different deformations, and the deformation has little effect on the particle size of cementite. The existence of HDI-hardening effects on plain medium carbon steel warm-rolled and annealed samples was also verified by calculating the grain boundary strengthening method according to the ROM rule. The increase of elongation of annealed samples is attributed to the multi-stage regulation of ferrite recrystallization and cementite distribution, and the combination of HDI mechanism, grain boundary strengthening and Orowan strengthening mechanism is realized.
  - Various models are used to fit the true stress-true strain relationship. Various models were used to fit the stress-strain, and the Voce-Kocks model accurately described the stress-strain of plain medium carbon steel with a heterogeneous laminar structure, which can provide a theoretical reference for modeling heterogeneous lamellar structures. The warm rolling combined with short-term annealing process avoids the addition of expensive alloying elements and complex processing technology, which has the advantage of low cost and is suitable for industrial production.

#### ACKNOWLEDGMENTS

The authors gratefully acknowledge financial supports from the National Science Foundation of China (NSFC) (Nos.51974134), Major Science and Technology Special Project of Hebei Province (No. 21281008Z).

#### CONFLICT OF INTEREST

On behalf of all authors, the corresponding author states that there is no conflict of interest.

#### REFERENCES

- S. Mridha. *Reference Module in Materials Science and Materials Engineering*, 2016.
- X. Li and K. Lu: *Nat. Mater.*, 2017, vol. 16, pp. 700–01.
- X. Li and K. Lu: *Science*, 2019, vol. 364, pp. 733–34.
- X.L. Wu and Y.T. Zhu: *Mater Res Lett.*, 2017, vol. 5, pp. 527–32.
- X. Wu, M. Yang, F. Yuan, G. Wu, Y. Wei, X. Huang, and Y. Zhu: *Proc. Natl. Acad. Sci. USA*, 2015, vol. 112, pp. 14501–05.
- X.L. Wu, P. Jiang, L. Chen, J.F. Zhang, F.P. Yuan, and Y.T. Zhu: *Mater. Res. Lett.*, 2014, vol. 2, pp. 185–91.
- M. Calcagnotto, Y. Adachi, D. Ponge, and D. Raabe: *Acta Mater.*, 2011, vol. 59, pp. 658–70.
- B.Q. Han, J.Y. Huang, Y.T. Zhu, and E.J. Lavernia: *Acta Mater.*, 2006, vol. 54, pp. 3015–24.
- S. Suresh: *Science*, 2001, vol. 292, pp. 2447–51.
- Y. Zhu, K. Ameyama, P.M. Anderson, I.J. Beyerlein, H. Gao, H.S. Kim, E. Lavernia, S. Mathaudhu, H. Mughrabi, R.O. Ritchie, N. Tsuji, X. Zhang, and X. Wu: *Mater. Res. Lett.*, 2020, vol. 9, pp. 1–31.
- X.L. Wu, Y.T. Zhu, and K. Lu: *Scr. Mater.*, 2020, vol. 186, pp. 321–25.
- L. Zhang, Z. Chen, Y. Wang, G. Ma, T. Huang, G. Wu, and D.J. Jensen: *Scr. Mater.*, 2017, vol. 141, pp. 111–14.
- J.J. Sun, T. Jiang, Y.J. Wang, S.W. Guo, and Y.N. Liu: *Mater. Sci. Eng. A.*, 2018, vol. 734, pp. 311–17.
- G. Niu, H.B. Wu, D. Zhang, N. Gong, and D. Tang: *Metals.*, 2017, vol. 7, p. 316.
- W.Y. Guo, J. Li, and X.F. Jiang: *J. Mater. Eng. Perform.*, 2011, vol. 21, pp. 1003–07.
- H. Ghiabakloo and M. Kazeminezhad: *Met. Mater. Int.*, 2017, vol. 23, pp. 984–93.
- C. Ji, L. Wang, and M.-Y. Zhu: *J. Iron Steel Res. Int.*, 2015, vol. 22, pp. 1031–36.
- M. Pérez: *Mater. Sci. Eng. A.*, 2017, vol. 690, pp. 303–12.
- M. Perez: *Scr Mater.*, 2005, vol. 52, pp. 709–12.
- J.L. Ning, E. Courtois-Manara, L. Kurmanaeva, A.V. Ganeev, R.Z. Valiev, C. Kubel, and Y. Ivanisenko: *Mater. Sci. Eng. A.*, 2013, vol. 581, pp. 8–15.
- L. Storovejva, D. Ponge, R. Kaspar, and D. Raabe: *Acta Mater.*, 2004, vol. 52, pp. 2209–20.
- D.A. Hughes, N. Hansen, and D.J. Bammann: *Scr. Mater.*, 2003, vol. 48, pp. 147–53.
- Q. Liu and N. Hansen: *Scr. Metall. Mater.*, 1995, vol. 32, pp. 1289–95.
- H. Gao, Y. Huang, W.D. Nix, and J.W. Hutchinson: *J. Mech. Phys. Solids.*, 1999, vol. 47, pp. 1239–63.
- L.P. Kubin and A. Mortensen: *Scr. Mater.*, 2003, vol. 48, pp. 119–25.
- C. Yang: *Int. J. Mech. Sci.*, 2006, vol. 48, pp. 950–57.
- Y. Jiang, R. Xu, Z. Tan, G. Ji, G. Fan, Z. Li, D. Xiong, Q. Guo, Z. Li, and D. Zhang: *Carbon*, 2019, vol. 146, pp. 17–27.
- J.H. Zhou, Y.F. Shen, Y.Y. Hong, W.Y. Xue, and R.D.K. Misra: *Mater. Sci. Eng. A.*, 2020, vol. 769, p. 138471.
- K.S. Cho, S.S. Park, D.H. Choi, and H. Kwon: *Alloys Compd.*, 2015, vol. 626, pp. 314–22.
- Y.F. Wang, M.S. Wang, K. Yin, A.H. Huang, and C.X. Huang: *Trans. Nonferr. Met. Soc.*, 2019, vol. 29, pp. 588–94.
- W. Morrison: *ASM Trans. Quart.*, 1966, vol. 59, pp. 824–46.
- S.-I. Lee, S.-H. Shin, and B. Hwang: *Metals.*, 2021, vol. 11, p. 1314.
- H.K. Sung, D.H. Lee, S. Lee, H.S. Kim, Y. Ro, C.S. Lee, B. Hwang, and S.Y. Shin: *Metall. Mater. Trans. A.*, 2016, vol. 47A, pp. 2726–38.
- S.-I. Lee, S.-Y. Lee, S.G. Lee, H.G. Jung, and B. Hwang: *Met. Mater. Int.*, 2018, vol. 24, pp. 1221–31.
- G.I. Taylor: *Proc. R. Soc. Lond.*, 1934, vol. 145, pp. 362–87.
- N. Hansen and X. Huang: *Acta Mater.*, 1998, vol. 46, pp. 1827–36.

37. X. Liu, Z. He, J. Ye, L. Yan, S. Li, and Y. Tang: *J. Constr. Steel Res.*, 2020, vol. 173, 106232.
38. S.S. Sohn, H. Song, B.-C. Suh, J.-H. Kwak, B.-J. Lee, N.J. Kim, and S. Lee: *Acta Mater.*, 2015, vol. 96, pp. 301–10.
39. L.A. Zepeda-Ruiz, A. Stukowski, T. Ooppelstrup, N. Bertin, N.R. Barton, R. Freitas, and V.V. Bulatov: *Nat. Mater.*, 2021, vol. 20, pp. 315–20.
40. J.H. Hollomon: *Met. Technol.*, 1945, vol. 12, pp. 268–90.
41. M.S. Mohsenzadeh and M. Mazinani: *Mater. Sci. Eng. A.*, 2017, vol. 702, pp. 113–24.
42. M.S. Mohsenzadeh and M. Mazinani: *Mater. Sci. Eng. A.*, 2016, vol. 673, pp. 193–203.
43. P. Ludwik: *Elemente der Technologischen Mechanik*, Springer-Verlag, Berlin, 1909.
44. H.W. Swift: *J. Mech. Phys. Solids.*, 1952, vol. 1, pp. 1–8.
45. S.K. Samanta: *Int. J. Mech. Sci.*, 1968, vol. 10, pp. 613–36.
46. E. Voce: *J. Inst. Met.*, 1948, vol. 74, pp. 537–62.
47. E. Voce: *Metallurgia*, 1955, vol. 51, pp. 219–26.
48. Z. Misiolok, J. Kowalczyk, and P. Kastner: *Arch. Hutn.*, 1977, vol. 22, pp. 71–88.

**Publisher's Note** Springer Nature remains neutral with regard to jurisdictional claims in published maps and institutional affiliations.

Springer Nature or its licensor (e.g. a society or other partner) holds exclusive rights to this article under a publishing agreement with the author(s) or other rightsholder(s); author self-archiving of the accepted manuscript version of this article is solely governed by the terms of such publishing agreement and applicable law.